PHYSICS

Ergodicity breaking in rapidly rotating C_{60} fullerenes

Lee R. Liu[1,2]*, Dina Rosenberg[1,2], P. Bryan Changala[1,2]†, Philip J. D. Crowley[3], David J. Nesbitt[1,2,4], Norman Y. Yao[3], Timur V. Tscherbul[5], Jun Ye[1,2]*

Ergodicity, the central tenet of statistical mechanics, requires an isolated system to explore all available phase space constrained by energy and symmetry. Mechanisms for violating ergodicity are of interest for probing nonequilibrium matter and protecting quantum coherence in complex systems. Polyatomic molecules have long served as a platform for probing ergodicity breaking in vibrational energy transport. Here, we report the observation of rotational ergodicity breaking in an unprecedentedly large molecule, $^{12}C_{60}$, determined from its icosahedral rovibrational fine structure. The ergodicity breaking occurs well below the vibrational ergodicity threshold and exhibits multiple transitions between ergodic and nonergodic regimes with increasing angular momentum. These peculiar dynamics result from the molecule's distinctive combination of symmetry, size, and rigidity, highlighting its relevance to emergent phenomena in mesoscopic quantum systems.

Isolated systems that break ergodicity have been explored in a variety of experimental settings, including spin glasses (*1*), ultracold neutral atoms (*2*, *3*) and ions (*4*), and photonic crystals (*5*). These systems exhibit ergodicity breaking of spin configurations and momentum or spatial distributions. By contrast, gas-phase polyatomic molecules provide opportunities to probe the ergodicity breaking of collective (rotational and vibrational) excitations in a finite quantum system. In this context, a topic of major interest has been the transport of energy deposited into molecular vibrations by optical pumping or collisions. Intramolecular vibrational redistribution (IVR) sets in once a critical threshold, defined by the product of vibrational coupling and the local density of vibrational states (which has a power-law scaling with vibrational energy), is exceeded (*6*–*11*). This vibrational ergodicity transition has been studied vigorously in the context of understanding and controlling unimolecular reaction dynamics (*12*).

Among polyatomic molecules, buckminsterfullerene ($^{12}C_{60}$) is notable for its structural rigidity and high degree of symmetry, which suppress IVR and allow for spectroscopic resolution (*13*) and optical pumping (*14*) of individual rovibrational states—an unusual and fortuitous situation for a molecule with 174 vibrational modes. Its small rotational constant and stiff, cage-like structure ensure that hundreds of rotational states are populated even when vibrational excitations are largely frozen out, which can be achieved with modest buffer gas cooling to ~120 K. Thus, a thermal ensemble of $^{12}C_{60}$ can reveal extensive, state-resolved rotational perturbations spanning hundreds of rotational quanta by eliminating vibrational "hot bands."

First observed and understood in atomic nuclei (*15*–*22*), rotational perturbations can arise from spherical symmetry breaking in the frame fixed to a rotating self-bound deformable body (*23*), which lifts the degeneracy of different body-fixed projections of the total angular momentum vector **J**. Such perturbations, also called "tensor interactions" because of their anisotropic nature, manifest in fine-structure splitting of the total angular momentum (J) multiplets in rovibrational spectra and encode rich dynamics such as rotational bifurcations (*18*, *24*), as previously observed in tetrahedral SnH_4, CD_4, CF_4, SiH_4, and SiF_4 and octahedral SF_6 molecules (*25*–*33*). Nevertheless, observing icosahedral tensor interactions, first predicted for $^{12}C_{60}$ over three decades ago (*34*), has remained an elusive goal, because there are far fewer examples of icosahedral molecules, nonspherical interactions occur only at higher orders of interactions, and icosahedral molecules are necessarily larger than lower-symmetry spherical top molecules, implying a smaller rotational constant.

In this work, we observed these icosahedral tensor interaction splittings, revealing rotational ergodicity transitions in $^{12}C_{60}$ at energies well below its IVR threshold (*10*). Specifically, as the molecule "spins up" to higher J, the dynamics of the angular momentum vector J in the molecule-fixed frame switches between ergodic and nonergodic regimes. In the nonergodic regime, distinct vector **J** trajectories exist in the same energy range but remain separated by energy barriers. In the limit of high J, the tunneling between these trajectories is too weak to restore ergodicity, leaving a characteristic signature in the fine-structure level statistics. This phenomenon differs from IVR in three key respects: (i) It involves the "transport" of the molecule frame orientation of vector **J** instead of vibrational energy; (ii) it can occur well below the IVR threshold; and (iii) it switches back and forth multiple times between ergodic (described by a 6th rank tensor interaction) and nonergodic (described by a 10th rank tensor interaction) regimes as the angular momentum is varied. This peculiar dynamical behavior arises from multiple avoided crossings with other vibrational states, which induce nonmonotonic variations in the molecule's anisotropic character as J is varied. The rotational ergodicity transitions bear some similarity to those studied in asymmetric top molecules in a static electric field (*35*, *36*) in that both concern the transport of angular momentum in the molecule frame. However, unlike in (*35*, *36*), the rotational ergodicity transitions in $^{12}C_{60}$ are induced by intramolecular rovibrational coupling in the freely rotating molecule, rather than by an externally applied electric field.

Effective $^{12}C_{60}$ rovibrational Hamiltonian

The rovibrational structure of C_{60} can be described by a field-free molecular Hamiltonian

$$H = H_{\text{scalar}} + H_{\text{tensor}} \quad (1)$$

The scalar Hamiltonian H_{scalar} contains only those combinations of vector **J** and vibrational angular momentum ℓ that preserve their spherical degeneracy (*37*)

$$H_{\text{scalar}} = \nu_0 + B\mathbf{J}^2 + D\mathbf{J}^4 + \cdots - 2B\zeta\mathbf{J}\cdot\ell \quad (2)$$

where ν_0 is the vibrational band origin, B is the rotational constant, D is the scalar centrifugal distortion constant, and ζ is the Coriolis coupling constant.

Rovibrational fine structure is encoded in the tensor Hamiltonian H_{tensor}. For simplicity, we considered a pure rotational tensor Hamiltonian consisting of the two lowest-order "icosahedral invariants." These invariants are linear combinations of spherical tensors of the same rank that transform according to the totally symmetric irreducible representation in the icosahedral point group (I_h) (*38*). They can be expressed (*39*) in the basis of spherical harmonics $Y_q^k(\theta,\phi)$ of degree k and order q, which depend explicitly on the molecular frame's polar θ and azimuthal ϕ angles (Fig. 1A). The first two nontrivial (anisotropic) icosahedral invariants, with ranks 6 and 10, are given by

$$T^{[6]}(\theta,\phi) = \frac{\sqrt{11}}{5}Y_0^6(\theta,\phi) + \frac{\sqrt{7}}{5}\left(Y_5^6(\theta,\phi) - Y_{-5}^6(\theta,\phi)\right) \quad (3)$$

[1]JILA, National Institute of Standards and Technology and University of Colorado, Boulder, CO 80309, USA. [2]Department of Physics, University of Colorado, Boulder, CO 80309, USA. [3]Department of Physics, Harvard University, Cambridge, MA 02135, USA. [4]Department of Chemistry, University of Colorado, Boulder, CO 80309, USA. [5]Department of Physics, University of Nevada, Reno, NV 89557, USA.
*Corresponding author. Email: lee.richard.liu@gmail.com (L.R.L.); ye@jila.colorado.edu (J.Y.)
†Present address: Center for Astrophysics, Harvard and Smithsonian, Cambridge, MA 02138, USA.

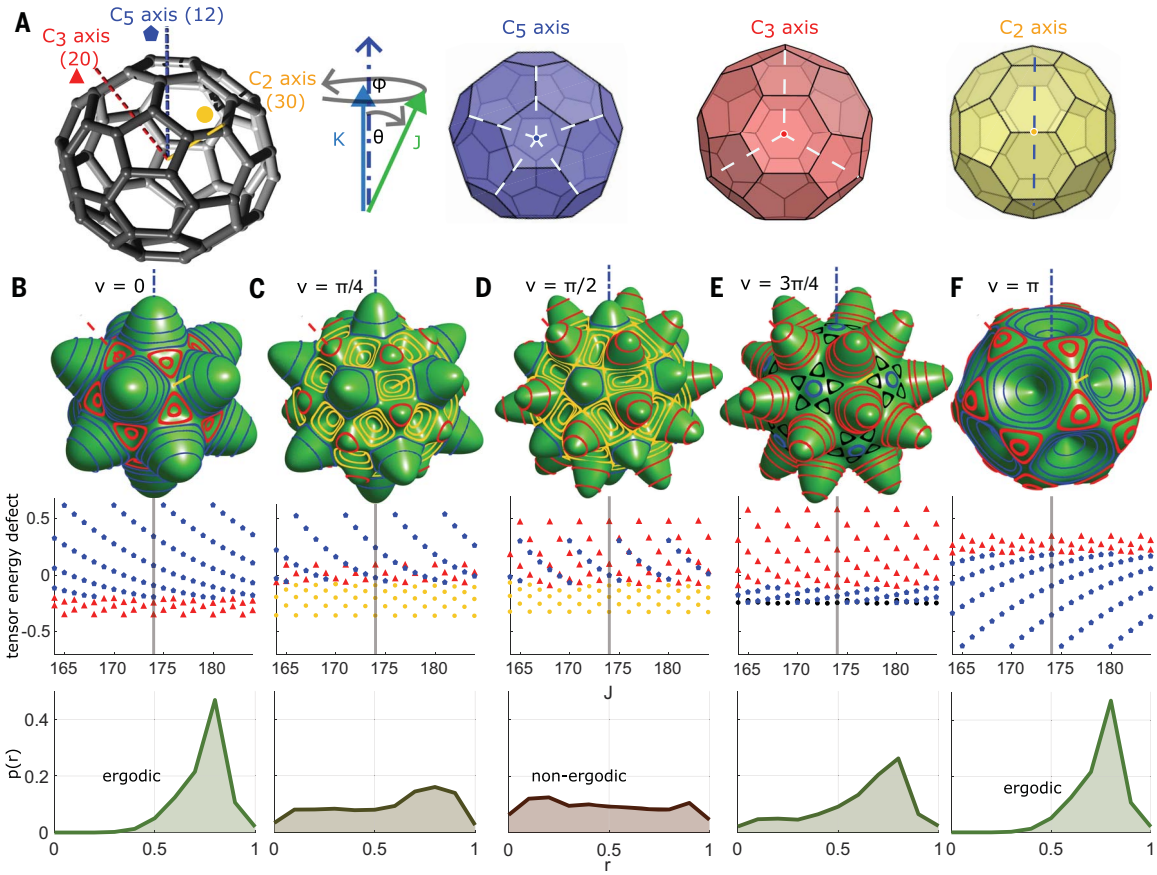

Fig. 1. Rotational energy surfaces and eigenvalues corresponding to icosahedral invariant spherical tensors. (**A**) Symmetries of C_{60}. (Left to right) (1) Ball-and-stick model of C_{60}, with the three different types of rotational symmetry axes that label stationary points on the rotational energy surface (RES). The degeneracies of the stationary points are listed in parentheses. Color and plot marker coding for each type of rotational symmetry axis are shown. (2) Body-fixed coordinates: polar θ and azimuthal ϕ angles. (3–5) View along C_5, C_3, and C_2 rotational symmetry axes. (**B** to **F**) (Top panels) RESs, defined by their radii $r(\theta,\phi) = 1 + H^{(6+10)}_{\text{tensor}}(\nu;\theta,\phi)/2$, for ν ranging from 0 to π. Eigenvalues of $1 + H^{(6+10)}_{\text{tensor}}(\nu)/2$ calculated for the fully symmetrized $J = 174$ subspace are plotted on the surface as radial contours, colored corresponding to their dominant rotational symmetry character. (Center panels) Tensor energy defects [eigenvalues of $H^{(6+10)}_{\text{tensor}}(\nu)$] over a range of J. The gray vertical line highlights $J = 174$. Eigenvalues are plotted using the marker corresponding to their dominant C_5, C_3, or C_2 character (A). Near the separatrices, the assignment is somewhat ambiguous owing to strong mixing. (Bottom panels) Distribution $p(r)$ of energy gap ratios r (see text) calculated from tensor energy defect spectra aggregated over J = 0 to 400. Away from $\nu = 0, \pi$ [(C) to (E)], the finite value of $p(r)$ as $r \to 0$ is a signature of ergodicity breaking.

$$T^{[10]}(\theta,\phi) = \frac{\sqrt{3\cdot 13\cdot 19}}{75} Y^{10}_{0}(\theta,\phi) - \frac{\sqrt{11\cdot 19}}{25}\left(Y^{10}_{5}(\theta,\phi) - Y^{10}_{-5}(\theta,\phi)\right) + \frac{\sqrt{3\cdot 11\cdot 17}}{75}\left(Y^{10}_{10}(\theta,\phi) + Y^{10}_{-10}(\theta,\phi)\right) \quad (4)$$

which are combined to construct a truncated tensor Hamiltonian

$$H^{(6+10)}_{\text{tensor}} = \gamma\left(\cos\nu T^{[6]} + \sin\nu T^{[10]}\right) \quad (5)$$

This Hamiltonian is parameterized by an overall scaling factor γ and mixing angle ν such that $\nu = 0$ and $\nu = \pi/2$ correspond to pure $T^{[6]}$ and pure $T^{[10]}$, respectively.

All operators that are incompatible with icosahedral point group symmetry, including any spherical harmonics of rank 1 to 5, 7 to 9, 11, 13, 14,... (*40*), vanish from the Hamiltonian. The use of full rovibrational tensor operators is unlikely to change the picture qualitatively, particularly when J (~100 to 300) is much greater than the vibrational angular momentum quantum number $\ell = 1$ (*38*). These polyhedral invariants are similar to those used to describe the crystal field splitting of electronic orbitals owing to an external lattice environment (*41*) or the ligand field splitting in transition-metal complexes (*42*).

The energetic correction, or tensor energy defect, associated with orienting **J** in different directions in the molecule frame can be visualized by the altitude of a semi-classical "rotational energy surface" (RES), defined at a fixed J. Various possible icosahedral RESs, defined by their radii $r(\theta,\phi) = 1 + H^{(6+10)}_{\text{tensor}}(\nu;\theta,\phi)/2$, corresponding to different mixing angles ν, are plotted for $J = 174$ in the top panels of Fig. 1, B to F. Stationary points always lie on C_2, C_3, or C_5 rotational symmetry axes. However, as ν varies, they change in character between minima, maxima, and saddle points. The RES dictates the dynamics of **J** in the molecule frame (*30*, *43*–*46*), analogous to how an adiabatic potential energy surface steers the relative motions of nuclei (*47*). During free evolution, the trajectory of **J** follows an equipotential contour of the RES.

In a full quantum-mechanical treatment, the perturbation $H^{(6+10)}_{\text{tensor}}$ leads only to discrete tensor energy defects e_i given by the eigenvalues of $H^{(6+10)}_{\text{tensor}}$ in a fully symmetrized fixed-J subspace. These orbits trace out the closed contours on the RES in Fig. 1. The orbits may also be obtained directly from the RES: They are the trajectories that both (i) satisfy a Bohr quantization condition (*44*, *48*) and (ii) transform according to the totally symmetric irreducible representation of the icosahedral point group (*38*). The latter condition accounts for the

quantum indistinguishability of each bosonic nucleus in the $^{12}C_{60}$ isotopolog (*13*, *49*) and is analogous to the selection of odd or even rotational states in ortho- or para-hydrogen molecules, respectively. The tensor energy defects are plotted for a range of J in the center panels of Fig. 1, B to F, and may be expected to appear in the rovibrational fine structure of $^{12}C_{60}$.

Resolving $^{12}C_{60}$ rovibrational fine structure

In the preceding discussions, we have focused solely on the geometric effects of icosahedral symmetry. In general, however, the measured tensor defect spectra may exhibit additional J-dependent scaling and offsets, which depend on intramolecular couplings specific to $^{12}C_{60}$. To resolve rovibrational perturbations in $^{12}C_{60}$, in this work, we explored the P-branch region of the 1185 cm^{-1} T_{1u} (3) band, first identified as a region of potential interest in (*13*). Using cavity-enhanced continuous-wave (cw) spectroscopy with a quantum cascade laser (QCL) source, we achieved a minimum absorption sensitivity $\alpha_{min} = 2.1 \times 10^{-10} cm^{-1}\ Hz^{-1/2}$, or 1000-fold better detection sensitivity per spectral element than in (*13*) ($\alpha_{min} = 2.2 \times 10^{-7}$ $cm^{-1}\ Hz^{-1/2}$ per comb mode). We acquired 600-MHz-wide absorption spectra by simultaneously scanning the QCL frequency and free spectral range of the enhancement cavity across molecular absorption lines, and recording the frequency-dependent absorption. These spectra were stitched together by a combination of direct calibration of the QCL frequency with a Fourier transform spectrometer and comparison to matching spectral features in the broadband, low signal-to-noise (SNR) frequency comb spectrum of (*13*). We obtained an absolute frequency accuracy of ~6 MHz throughout the entire measured frequency range, limited by the resolution of the reference frequency comb spectrum. Finally, to ensure consistency of the absorption signal over multiple days of data collection, we have periodically remeasured the molecular absorption feature at R($J = 181$) at $\nu = 1186.27\ cm^{-1}$ and normalized all data taken around the same time to its line strength and measured cavity finesse.

Assigning $^{12}C_{60}$ rovibrational fine structure

The culmination of these efforts is the infrared spectrum in Fig. 2, spanning the spectral region from 1182.0 to 1184.7 cm^{-1}. At $J \lesssim 70$, there is a regular progression of rotational lines, similar to those in the R-branch (*13*). They rapidly split into intricate patterns before merging at and beyond $J \approx 300$. Zooming into the region labeled B), the rotational line centers could be fit to the scalar part of Eq. 1, as was done in (*13*).

$$\nu^P(J) = \nu_0 + B'(J-1)(J+2\zeta) - B''J(J+1) \quad (6)$$

where J here refers to the ground-state total angular momentum. The scalar centrifugal distortion term was not significant at our spectral precision and range of J. The fit yielded B'' = 0.0028 cm^{-1} for the ground-state rotational constant, $B' = B'' - 2.876 \times 10^{-7}\ cm^{-1}$ for the excited-state rotational constant, $\zeta = -0.37538$ for the Coriolis coupling constant, and $\nu_0 = 1184.85\ cm^{-1}$. Equation 6 yields a progression of rotational lines with a spacing of $\sim 2B(1-\zeta)$, where $B = (B' + B'')/2$. The spectroscopic constants were underdetermined and only served to facilitate J-assignment of the peaks in a manner consistent with the R-branch assignments of (*13*). The extrapolated P-branch spectral line positions based on this scalar fit are plotted as gray vertical lines in Fig. 2, B to F, with every fifth J value labeled in red. The agreement with the measured line positions is excellent in the region $J < 70$, where the spectrum appears unperturbed (Fig. 2B).

To confirm our J assignment, we compared the peak absorption cross sections to the nuclear spin weights of the ground-state rotational levels and found that they match well. Finally, we applied a frequency-dependent scaling factor to the raw absorption spectrum $(2J+1)^{-1} e^{B'J(J+1)/k_B T}$. This scaling removes the effects of lab frame angular momentum degeneracy and the thermal ensemble, emphasizing the dynamics in the molecule-fixed frame.

The peaks were identified manually and circled in blue. Figure 2, C and D, show two representative regions, at $J \sim 90$ and $J \sim 170$, respectively, where peaks could still be individually resolved. The local peak density again matches the predicted nuclear spin weights (in blue), confirming that the rovibrational

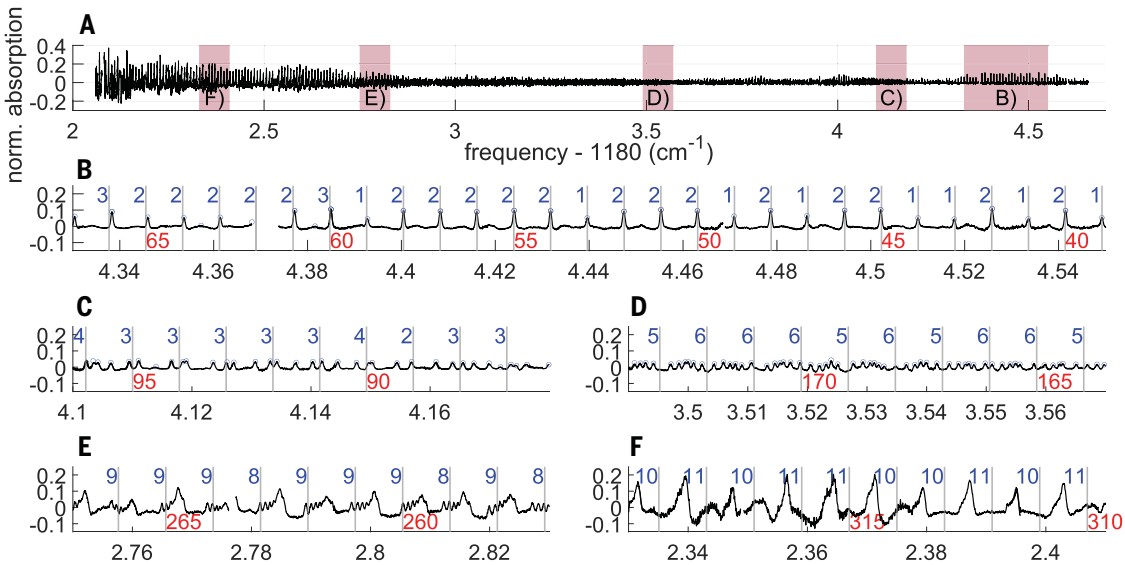

Fig. 2. Direct continuous-wave (cw) absorption spectroscopy of C_{60} P-branch. (**A**) Complete normalized cw spectrum of P-branch to expose the J dependence of the nuclear spin weights. Red highlighted regions are shown in greater detail in subsequent panels. (**B** to **F**) Enlargement of red highlighted regions in (A). (B) Enlargement of low-J region of the P-branch. This relatively unperturbed region of the P-branch is fit to a rigid-rotor Hamiltonian to obtain the rotational spacing $2B(1-\zeta)$. Fitted line positions are indicated by the gray vertical grid lines, with J labeled in red. Blue numbers denote calculated nuclear spin weights, which match the measured peak intensities well. In (C) and (D), peaks are resolvable and marked with blue circles. In (E) and (F), spectral congestion prohibits identification of individual peaks.

fine-structure splitting originates from icosahedral tensor interactions of Eq. 5 that lift K-degeneracy. Figure 2, E and F, show two regions where the peaks have begun to merge, and individual peaks can no longer be easily identified ($J > 247$).

Interpreting the tensor splittings requires assigning each absorption peak to a particular J. We began by assigning each peak to its nearest J value according to the scalar fit of Eq. 6. Subtracting the scalar contribution (Eq. 6) from the central frequency of each peak generated a single "period" of a Loomis-Wood-like defect plot in Fig. 3A. There remains some ambiguity in the defect assignments, as illustrated in the inset of Fig. 3A: Each defect is constrained to the line with slope $2B(1-\zeta)$, which passes through its current position.

By carefully rearranging individual defects according to these discrete allowed "moves," we unwrapped five distinct regions that exhibit continuous-looking patterns (Fig. 3B). Because of the discontinuities at $J \simeq 80$, 110, 160, and 220, there was still some ambiguity in the overall shift of the four perturbed sections labeled (i) to (iv). To remove this ambiguity, we recognized each section's dominant pure-rank tensor character as follows: (i) $-T^{[6]}$; (ii) $T^{[10]}$; (iii) $T^{[6]}$; (iv) $-T^{[6]}$. Eigenvalue spectra in Fig. 1, B, D, and F, show that the extremal eigenvalues associated with C_n rotational symmetry axes occur when J is an integer multiple of n. The J-assignment depicted in Fig. 3B satisfies this condition for all sections simultaneously. This final J-assignment was confirmed by the excellent agreement between J-resolved peak counts and calculated nuclear spin weight far from the discontinuities Fig. 3C.

Rotational ergodicity transitions

The J-dependent tensor energy defects imply rovibrational dynamics of $^{12}C_{60}$. To infer these dynamics, we parameterized each of the four perturbed regions (i) to (iv) in Fig. 3B in terms of a mixed tensor (Eq. 5), J-dependent scaling $b(J)$, and J-dependent scalar offset $a(J)$:

$$a(J) + b(J) \times e(\nu; J, K) \qquad (7)$$

where $e(\nu; J, K)$ are the J-dependent tensor splittings as plotted in the lower panels of Fig. 1, B to F.

First, $a(J)$ was obtained from the observed mean defect of each section. Next, by performing a point-cloud registration (*50–52*) to the theoretical eigenvalue spectra and the measured defect plot, we assigned a best-fit mixing angle ν to each section: (i) π; (ii) 0.45π; (iii) 1.9π; and (iv) π (*38*). Finally, $b(J)$ was obtained from a least-squares fit to a polynomial in J (*38*). The resulting reconstructed defect plot for regions (i) to (iv) is shown in Fig. 3D.

The abrupt changes in mixing angles ν are associated with transitions between ergodic and nonergodic rotational dynamics as the molecule "spins up" to higher J. These dynamics

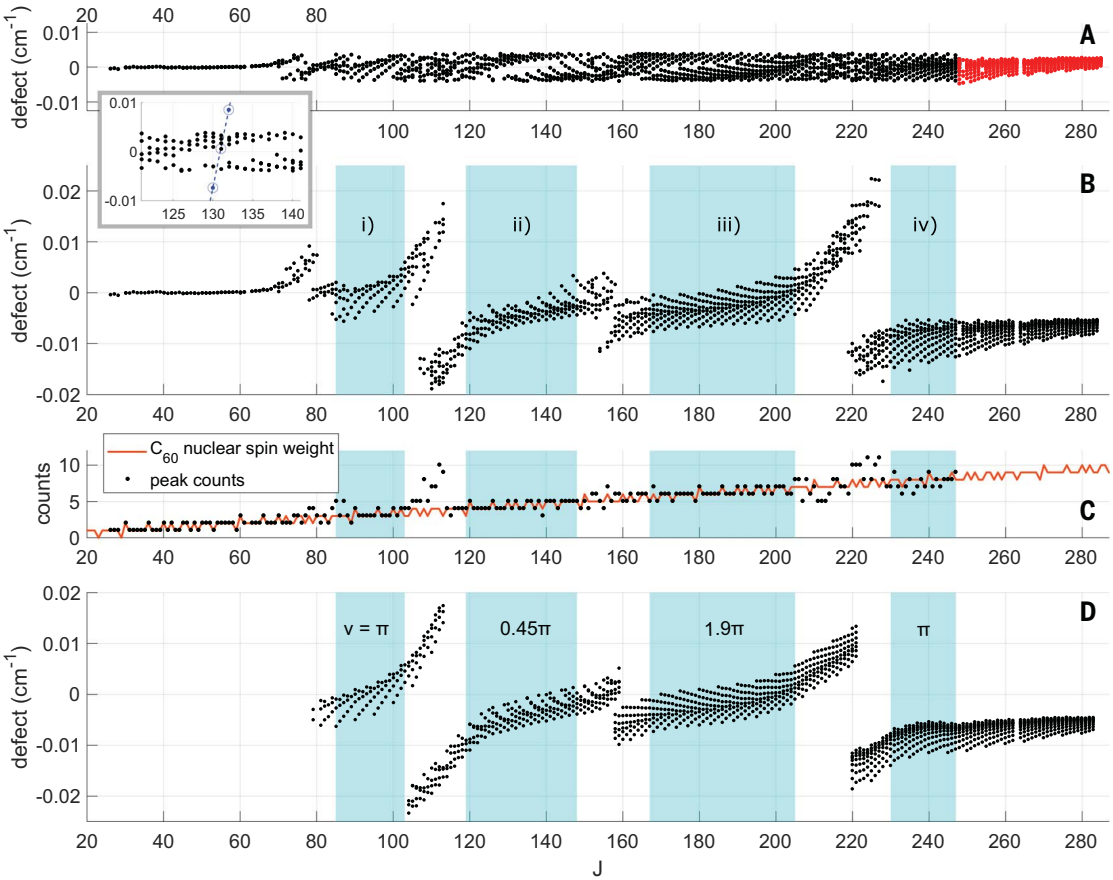

Fig. 3. Obtaining P-branch tensor energy defects versus *J*. (**A**) Plot of experimental energy defects from nearest-neighbor J assignment. Peaks are assigned to nearest J according to rigid rotor model (gray vertical grid lines in Fig. 2, B to F). Red defect points ($J > 247$) correspond to peaks in the absorption spectrum that are no longer individually resolved. Their peak centers are obtained from fitting to a cluster of Voigt lineshapes (*38*). (Inset) Unwrapping procedure follows a series of allowed "moves" that simultaneously translate points in vertical steps of $\pm 2B(1-\zeta)$ and horizontal steps of ±1. (**B**) "Unwrapped" defect plot. Four avoided crossings with varying strengths are seen at $J \simeq 80$, 110, 160, and 220. Defect patterns resemble eigenvalue spectra of icosahedral invariant tensors. (**C**) Calculated nuclear spin weights overlaid with measured peak counts. Blue highlighted sections show excellent agreement between calculated nuclear spin weights of C_{60} and assigned peak counts. (**D**) Reconstruction of perturbed sections of P-branch spectrum based on eigenvalue spectra of mixed tensor operator $H^{(6+10)}_{\text{tensor}}(\nu)$. Four perturbed portions of (B) are reproduced with four mixing angles ν.

transition from ergodic for region (i), to nonergodic for region (ii), and back again for regions (iii) and (iv).

The origin of this ergodicity breaking can be understood semi-classically using the RESs in Fig. 1, B, D, and F. The dynamics of vector **J** are ergodic when time evolution explores the full space of symmetry-allowed states at the same energy. For region (iii), the dominant tensor character is $T^{[6]}$. Naïvely, the existence of 12 disconnected trajectories encircling the C_5 axes breaks ergodicity. However, these trajectories cannot be distinguished in $^{12}C_{60}$: Owing to the indistinguishability of the ^{12}C nuclei, all 12 semi-classical trajectories correspond to a single quantum state given by their fully symmetric superposition. As such, the vector **J** dynamics do explore the full range of states at a given energy, and hence are ergodic. The same argument applies for regions (i) and (iv), which differ from (iii) only in the sign of tensor energy defects (Fig. 1F).

By contrast, for region (ii), the dominant tensor character is $T^{[10]}$. The C_5 and C_3 axes both correspond to peaks on the RES and to host trajectories over the same range of energies (Fig. 3D). Trajectories encircling the C_5 and C_3 axes are distinguishable, and hence correspond to distinct quantum states. The quantum tunneling between these trajectories is unable to restore the ergodicity: The tunneling integral between C_5 and C_3 is exponentially small in J (*53*, *54*), whereas the level spacing only scales as $1/J$. The scaling of the tunneling integral follows from standard Wentzel–Kramers–Brillouin (WKB) results (*55*), and the scaling of level spacings can be seen by comparing the relatively fixed bandwidth of tensor energy defects (Fig. 3B) with the nuclear spin weight $\sim(2J+1)/60$. Consequently, for our measured J (well within the large-J limit), tunneling corrections are typically only perturbative.

Energy-level statistics provide a simple probe of this ergodicity breaking in molecular spectra (*56*, *57*). Quantum ergodicity is associated with eigenstates extended in phase space that can be strongly coupled by local perturbations, inducing energy-level repulsion. By contrast, ergodicity breaking is associated with the existence of localized eigenstates, which are not strongly coupled by perturbations and whose energies are uncorrelated (*58*). Ergodic and nonergodic dynamics are therefore respectively associated with level repulsion and its absence (*59*). A useful diagnostic tool is the distribution $p(r)$, where r is the ratio of consecutive level spacings e_i (*60*, *61*):

$$r_i = \min\left(\frac{s_i}{s_{i-1}}, \frac{s_{i-1}}{s_i}\right) \tag{8}$$

$$s_i = e_{i+1} - e_i \tag{9}$$

In the limit of $r \to 0$, level repulsion in an ergodic system causes $p(r) \to 0$, and for a nonergodic system $p(r) \to$ constant. Similar energy-level statistics have been used to analyze systems as diverse as nuclear spectra (*59*), ultracold atomic scattering (*62*), and many-body localization (*63*).

Figure 4, A to C, show the energy-gap ratios computed from sections (i) to (iii), respectively, of the experimental defect plot (Fig. 3B). Here, sections (i) and (iii) exhibit persistent level repulsion characteristic of ergodicity, whereas section (ii) does not, indicating nonergodicity. We aggregated the energy-gap ratios over each one of sections (i) to (iii) and their respective distributions in Fig. 4, D to F. These distributions confirm the presence of level repulsion in sections (i) and (iii) and its absence in section (ii).

The physical origin of rovibrational tensor energy defects in $^{12}C_{60}$ can be inferred from Fig. 3B. The defects arise from rovibrational coupling between the bright P-type excited $T_{1u}^{(+)}(3)$ state and a background of perturbing dark states. Specifically, both the discontinuities and excess observed peaks at specific J values are characteristic of avoided crossings with perturbing zero-order dark vibrational combination states. As they cross $T_{1u}^{(+)}(3)$ from below, rovibrational coupling lifts the degeneracy of J multiplets in the $T_{1u}^{(+)}(3)$ state, imparting tensor character that depends on the identity of the perturbing vibrational state. The tensor character of the $T_{1u}^{(+)}(3)$ state (specifically the fitted ν values) is stable in between avoided crossings, suggesting that each of these sections is dominantly affected by just one perturbing state at a time. At the avoided crossings, this assumption breaks down, as made particularly evident by the rapid change in mixing angle just before and after the avoided crossing at $J = 160$ of Fig. 3B. There is no apparent structure to the changes in mixing angle and coupling strength induced by the different avoided crossings, suggesting that the perturbing dark states are distinct and not part of the same Coriolis manifold. Finally, using the observed local density of perturbing states $\rho_{obs} \approx 2/\text{cm}^{-1}$ and average measured vibrational coupling strength (bandwidth of the avoided crossings) of $\beta_{avg} \approx 2\times 10^{-2}\ \text{cm}^{-1}$ (*38*), we arrive at an IVR threshold parameter (*10*) $T(E) = \sqrt{2\pi/3}\rho_{obs}\beta_{avg} \approx 0.06 \ll 1$. Our $^{12}C_{60}$ rotational ergodicity transitions are observed well below the IVR threshold, a conclusion supported by the spectroscopically well-resolved $T_{1u}(3)$ band. This further highlights the fact that, although the rotational ergodicity transition relies on intramolecular vibrational coupling, it is completely distinct from IVR.

Conclusion

We have measured and characterized icosahedral tensor rovibrational coupling in $^{12}C_{60}$. Analysis of the spectrum of rovibrational tensor energy defects revealed that as the molecule is spun up to higher J, there is a series of transitions in the dynamical behavior of **J** in the fixed body frame. Specifically, vector **J** switches between ergodic and nonergodic behavior at particular J values, leaving a characteristic imprint on the defect-level statistics. These ergodicity transitions arise from dark vibrational combination states that cross the $T_{1u}^{(+)}(3)$ state at particular J values, transferring their anisotropic character onto the $T_{1u}^{(+)}(3)$ state through rovibrational coupling.

Our measurements open the door to a rich hierarchy of emergent behavior in C_{60} isotopologs, accessible at ever-higher spectral resolution. The small nuclear spin-rotation interaction—for example, in ^{13}C-substituted isotopologs of C_{60}—can have a magnified effect owing to the small superfine splittings near RES extrema.

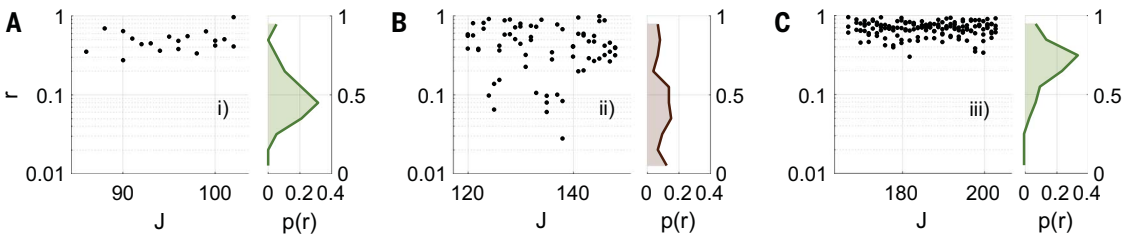

Fig. 4. Energy-level statistics in ergodic and nonergodic regimes. (**A** to **C**) (Left panels) Gap ratio r as a function of J calculated from sections (i) to (iv) of the defect spectrum (Fig. 3B). Gap ratios are only plotted at J values for which the peak counts match the calculated nuclear spin weight (Fig. 3C). (Right panels) Normalized distribution $p(r)$ of gap ratios aggregated over sections (i) to (iii). Note the change from logarithmic to linear r scale between left and right panels. Sections (i) and (iii) exhibit level repulsion, a signature of ergodicity, whereas section (ii) does not, indicating nonergodicity.

Such "hyperfine" coupling can lead to spontaneous symmetry breaking in a finite system (*31*, *64*). These insights could prove useful for exploiting the exotic orientation state space of C_{60} for quantum information processing (*65*) and for investigating the quantum-to-classical transition of information spreading (*66*). Ultimately, spectroscopy of C_{60} isotopologs at ever-higher spectral resolution promises to uncover deeper insights into the emergent dynamics of mesoscopic quantum many-body systems.

REFERENCES AND NOTES

1. K. Binder, A. P. Young, *Rev. Mod. Phys.* **58**, 801–976 (1986).
2. T. Kinoshita, T. Wenger, D. S. Weiss, *Nature* **440**, 900–903 (2006).
3. M. Schreiber *et al*., *Science* **349**, 842–845 (2015).
4. J. Smith *et al*., *Nat. Phys.* **12**, 907–911 (2016).
5. M. Segev, Y. Silberberg, D. N. Christodoulides, *Nat. Photonics* **7**, 197–204 (2013).
6. J. D. McDonald, *Annu. Rev. Phys. Chem.* **30**, 29–50 (1979).
7. G. M. Nathanson, G. M. Mcclelland, *J. Chem. Phys.* **81**, 629–642 (1984).
8. G. M. McClelland, G. M. Nathanson, J. H. Frederick, F. W. Farley, Excited States, E. C. Lim, K. K. Innes, eds. (Academic Press, Inc., 1988), vol. 7, pp. 83–106.
9. K. Sture, J. Nordholm, S. A. Rice, *J. Chem. Phys.* **61**, 203–223 (1974).
10. D. E. Logan, P. G. Wolynes, *J. Chem. Phys.* **93**, 4994–5012 (1990).
11. D. M. Leitner, *Entropy (Basel)* **20**, 673 (2018).
12. D. J. Nesbitt, R. W. Field, *J. Phys. Chem.* **100**, 12735–12756 (1996).
13. P. B. Changala, M. L. Weichman, K. F. Lee, M. E. Fermann, J. Ye, *Science* **363**, 49–54 (2019).
14. L. R. Liu *et al*., *PRX Quantum* **3**, 030332 (2022).
15. I. M. Pavlichenkov, *Sov. Phys. JETP* **55**, 5–12 (1982).
16. I. M. Pavlichenkov, B. I. Zhilinskii, *Ann. Phys.* **184**, 1–32 (1988).
17. Y. R. Shimizu, J. D. Garrett, R. A. Broglia, M. Gallardo, E. Vigezzi, *Rev. Mod. Phys.* **61**, 131–168 (1989).
18. I. M. Pavlichenkov, *Phys. Rep.* **226**, 173–279 (1993).
19. S. Frauendorf, *Rev. Mod. Phys.* **73**, 463–514 (2001).
20. H. Hübel, *Prog. Part. Nucl. Phys.* **54**, 1–69 (2005).
21. J. Kvasil, R. G. Nazmitdinov, *Phys. Rev. C Nucl. Phys.* **73**, 014312 (2006).
22. J. Kvasil, R. G. Nazmitdinov, A. S. Sitdikov, P. Veselý, *Phys. At. Nucl.* **70**, 1386–1391 (2007).
23. K. Fox, H. W. Galbraith, B. J. Krohn, J. D. Louck, *Phys. Rev. A Gen. Phys.* **15**, 1363–1381 (1977).
24. G. Pierre, D. A. Sadovskii, B. I. Zhilinskii, *Europhys. Lett.* **10**, 409–414 (1989).
25. R. S. McDowell *et al*., *J. Mol. Spectrosc.* **83**, 440–450 (1980).
26. C. W. Patterson, A. S. Pine, *J. Mol. Spectrosc.* **96**, 404–421 (1982).
27. J. P. Aldridge *et al*., *J. Mol. Spectrosc.* **58**, 165–168 (1975).
28. K. C. Kim, W. B. Person, D. Seitz, B. J. Krohn, *J. Mol. Spectrosc.* **76**, 322–340 (1979).
29. W. G. Harter, *J. Stat. Phys.* **36**, 749–777 (1984).
30. W. G. Harter, C. W. Patterson, *J. Math. Phys.* **20**, 1453–1459 (1978).
31. W. G. Harter, H. P. Layer, F. R. Petersen, *Opt. Lett.* **4**, 90–92 (1979).
32. R. S. McDowell, H. W. Galbraith, B. J. Krohn, C. D. Cantrell, E. D. Hinkley, *Opt. Commun.* **17**, 178–183 (1976).
33. J. Bordé, C. J. Bordé, *Chem. Phys.* **71**, 417–441 (1982).
34. W. G. Harter, D. E. Weeks, *Chem. Phys. Lett.* **132**, 387–392 (1986).
35. M. Abd El. Rahim, R. Antoine, M. Broyer, D. Rayane, P. Dugourd, *J. Phys. Chem. A* **109**, 8507–8514 (2005).
36. S. M. Pittman, E. J. Heller, *J. Phys. Chem. A* **119**, 10563–10574 (2015).
37. K. T. Hecht, *J. Mol. Spectrosc.* **5**, 355–389 (1961).
38. Materials and methods are available as supplementary materials.
39. Y. Zheng, P. C. Doerschuk, *Acta Crystallogr. A* **52**, 221–235 (1996).
40. P. R. Bunker, P. Jensen, *Mol. Phys.* **97**, 255–264 (1999).
41. K. R. Lea, M. J. Leask, W. P. Wolf, *J. Phys. Chem. Solids* **23**, 1381–1405 (1962).
42. B. J. S. Griffith, L. E. Orgel, *Q. Rev. Chem. Soc.* **11**, 381–393 (1957).
43. W. G. Harter, *Phys. Rev. A Gen. Phys.* **24**, 192–263 (1981).
44. W. G. Harter, C. W. Patterson, *J. Chem. Phys.* **80**, 4241–4261 (1984).
45. W. G. Harter, *Comput. Phys. Rep.* **8**, 319–394 (1988).
46. D. A. Sadovskii, B. I. Zhilinskii, J. P. Champion, G. Pierre, *J. Chem. Phys.* **92**, 1523–1537 (1990).
47. M. Khauss, *Annu. Rev. Phys. Chem.* **21**, 39–46 (1970).
48. W. G. Harter, D. E. Weeks, *J. Chem. Phys.* **90**, 4727–4743 (1989).
49. R. D. Johnson, G. Meijer, D. S. Bethune, *J. Am. Chem. Soc.* **112**, 8983–8984 (1990).
50. Y. Chen, G. Medioni, *Image Vis. Comput.* **10**, 145–155 (1992).
51. P. J. Besl, N. D. Mckay, *IEEE Trans. Pattern Anal. Mach. Intell.* **14**, 239–256 (1992).
52. A. V. Segal, D. Haehnel, S. Thrun, *Robot. Sci. Syst.* **5**, 435 (2010).
53. A. Auerbach, *Interacting electrons and Quantum magnetism* (Springer Science+Business Media, 1994).
54. J. L. van Hemmen, A. Sütö, *Europhys. Lett.* **1**, 481–490 (1986).
55. L. Landau, E. Lifshitz, Quantum Mechanics (Non-Relativistic Theory), vol. 3 (Pergamon Press, 1958).
56. M. V. Berry, M. Tabor, *Proc. R. Soc. London Ser. A* **356**, 375–394 (1977).
57. E. Abramson, R. W. Field, D. Imre, K. K. Innes, J. L. Kinsey, *J. Chem. Phys.* **80**, 2298–2300 (1983).
58. M. V. Berry, *Proc. R. Soc. London Ser. A* **413**, 183–198 (1987).
59. E. P. Wigner, *SIAM Rev.* **9**, 1–23 (1967).
60. V. Oganesyan, D. A. Huse, *Phys. Rev. B Condens. Matter Mater. Phys.* **75**, 155111 (2007).
61. Y. Y. Atas, E. Bogomolny, O. Giraud, G. Roux, *Phys. Rev. Lett.* **110**, 084101 (2013).
62. A. Frisch *et al*., *Nature* **507**, 475–479 (2014).
63. D. A. Abanin, E. Altman, I. Bloch, M. Serbyn, *Rev. Mod. Phys.* **91**, 021001 (2019).
64. J. Bordé *et al*., *Phys. Rev. Lett.* **45**, 14–17 (1980).
65. V. V. Albert, J. P. Covey, J. Preskill, *Phys. Rev. X* **10**, 031050 (2020).
66. C. Zhang, P. G. Wolynes, M. Gruebele, *Phys. Rev. A* **105**, 033322 (2022).
67. L. R. Liu *et al*., Supplementary data for ergodicity breaking in rapidly rotating C60 fullerenes, Harvard Dataverse (2023); https://doi.org/10.7910/DVN/E4KHWX [accessed 13 June 2023].

ACKNOWLEDGMENTS

We gratefully acknowledge comments on the manuscript from A. W. Young and Y.-C. Chan. **Funding:** This research was supported by AFOSR grant no. FA9550-19-1-0148; the National Science Foundation Quantum Leap Challenge Institutes (grant QLCI OMA-2016244); the National Science Foundation (grant Phys-1734006); and the National Institute of Standards and Technology. Support is also acknowledged from the US Department of Energy, Office of Science, National Quantum Information Science Research Centers, Quantum Systems Accelerator. D.R. acknowledges support from the Israeli council for higher education quantum science fellowship and is an awardee of the Weizmann Institute of Science–Israel National Postdoctoral Award Program for Advancing Women in Science. P.J.D.C. and N.Y.Y. acknowledge support from the AFOSR MURI program (FA9550-21-1-0069). D.J.N. acknowledges support from the US DOE (DE-FG02-09ER16021) and NSF (CHE 2053117). T.V.T. acknowledges support from the NSF EPSCoR RII Track-4 Fellowship no. 1929190. **Author contributions:** L.R.L., D.R., and J.Y. designed, discussed, and performed the experiment and analyzed the data. L.R.L., D.R., P.B.C., P.J.D.C., D.J.N., N.Y.Y., T.V.T., and J.Y. participated in theory discussions and calculations and in writing of the paper. **Competing interests:** None declared. **Data and materials availability:** Data for raw absorption spectra and unwrapped tensor energy defect plots are deposited in Harvard Dataverse (*67*). All other data needed to evaluate the conclusions in the paper are present in the paper or the supplementary materials.

SUPPLEMENTARY MATERIALS

science.org/doi/10.1126/science.adi6354
Supplementary Text
Figs. S1 to S3
Table S1
Reference (*68*)

Submitted 9 May 2023; accepted 23 June 2023
10.1126/science.adi6354